PHYSICS

Ferroicity-driven nonlinear photocurrent switching in time-reversal invariant ferroic materials

Hua Wang and Xiaofeng Qian*

Copyright © 2019 The Authors, some rights reserved; exclusive licensee American Association for the Advancement of Science. No claim to original U.S. Government Works. Distributed under a Creative Commons Attribution NonCommercial License 4.0 (CC BY-NC).

Nonlinear optical responses to external electromagnetic field, characterized by second- and higher-order susceptibilities, play crucial roles in nonlinear optics and optoelectronics. Here, we demonstrate the possibility to achieve ferroicity-driven nonlinear photocurrent switching in time-reversal invariant multiferroics. It is enabled by the second-order current response to electromagnetic field whose direction can be controlled by both internal ferroic orders and external light polarization. Second-order direct photocurrent consists of shift current and circular photocurrent under linearly and circularly polarized light irradiation, respectively. We elucidate the microscopic mechanism in a representative class of two-dimensional multiferroic materials using group theoretical analyses and first-principles theory. The complex interplay of symmetries, shift vector, and Berry curvature governs the fundamental properties and switching behavior of shift current and circular photocurrent. Ferroicity-driven nonlinear photocurrent switching will open avenues for realizing nonlinear optoelectronics, nonlinear multiferroics, etc., using the coupled ferroic orders and nonlinear responses of ferroic materials under external field.

INTRODUCTION

Nonlinear light-matter interaction plays a key role in the understanding, probing, and ultimate control of light and matter at the nanoscale. In particular, materials with strong nonlinear optical responses are highly desirable for many scientific disciplines and technological applications (*1*–*3*), e.g., ultrafast nonlinear optics (*4*), nonlinear biosensing and imaging (*5*), efficient generation of entangled photon pairs for quantum computing and quantum sensing (*6*, *7*), and all-optical transistor and computer (*8*–*10*). Because of the odd parity of the two polar vectors, electric dipole and electric field, even-order nonlinear electrical susceptibility tensors vanish in centrosymmetric crystals (*11*, *12*), while odd-order responses are not limited by this constraint.

Among a plethora of optical responses, nonequilibrium direct current (DC) from periodically driven system under light field is of particular interest. One notable example is linear photovoltaic Hall effect, which has been predicted in graphene (*13*). In addition, there exist appealing second-order nonlinear DC responses to electromagnetic field in noncentrosymmetric solids, e.g., shift current (SC) and circular photocurrent (CC). Both were recently observed in Weyl semimetals (*14*–*18*). In parallel, recent experiments suggest that two-dimensional (2D) van der Waals layered materials exhibit symmetry-dependent strong nonlinear optical responses, such as second and third harmonic generation. It makes nonlinear optical spectroscopy a perfect facile tool for characterizing and quantifying 2D materials, e.g., elastic strain, crystal orientation, phase transition, crystal thickness, even and odd layer oscillations, etc. Strong nonlinear responses in 2D materials also suggest their great advantage for phase-matching free nonlinear optics (*19*–*21*).

SC, known as bulk photovoltaic current (*22*, *23*), refers to a photoexcitation of an electron from the valence to the conduction band with a simultaneous change in the phase of wave functions. Another type of nonlinear photocurrent, CC—also known as injection current, circular photogalvanic effect (*24*, *25*)—arises from the interference of wave functions upon photoexcitation associated with a phase difference between two linearly polarized light, which allows for phase-modulated nonlinear photocurrent with tunable magnitude and direction. For example, left and right circularly polarized light can induce opposite currents. Using semiclassical Boltzmann framework, Moore and Orenstein (*26*) and Sodemann and Fu (*27*) revealed the fundamental root of nonlinear currents in Berry curvature induced anomalous velocity of metallic materials. This framework includes intraband process as the product of Berry phase and the gradient of Fermi-Dirac distribution function, equivalent to Berry curvature dipole (*27*). The nonlinear response in this case considers the intraband process in metallic systems at the low-frequency regime. In intrinsic semiconductors or insulators, the gradient of the Fermi-Dirac distribution vanishes and thus the Drude-like SC and CC responses also vanish. However, nonlinear photogalvanic current persists in noncentrosymmetric semiconductors because of the nonlinear interband process, which wasn't considered in the above intraband model.

Here, we demonstrate the possibility to achieve nonlinear photocurrent switching in time-reversal invariant multiferroics, namely, ferroicity-driven nonlinear photocurrent switching. More specifically, a Hall-like second-order direct photocurrent can be generated in time-reversal invariant systems upon electromagnetic field, whose direction can be facilely controlled by both internal ferroic orders and external light polarization and chirality. We provide a microscopic picture based on first-principles theory and group theoretical analysis of crystalline symmetry, time-reversal symmetry, permutation symmetry, gauge symmetry, and inherent causality. To illustrate the underlying mechanisms, we take monolayer group IV monochalcogenides [MX, with M = (Ge, Sn) and X = (S, Se, Te)], a ferroelectric-ferroelastic 2D multiferroics, as an example (*28*, *29*). Experimentally, Chang *et al.* (*28*) demonstrated that one of the MX compounds, atomic-thick SnTe, exhibits robust in-plane ferroelectricity at room temperature and that the application of voltage pulse between the scanning tunneling microscope tip and monolayer SnTe can manipulate the ferroelectric polarization through domain wall motion. Our previous theoretical study also demonstrated a wide range of kinetic barriers for coherent ferroic transition and domain wall energies (*29*). These experimental and theoretical studies suggested that it is possible to realize ferroelectric and ferroelastic switching in MX monolayers. In this work, using first-principles calculations and group theoretical analyses, we show that 2D MX monolayers exhibit large SC and CC responses that are dominated

Department of Materials Science and Engineering, Texas A&M University, College Station, TX 77843, USA.
*Corresponding author. Email: feng@tamu.edu

Downloaded from http://advances.sciencemag.org/ on January 17, 2021

by topological quantities, i.e., shift vector and Berry curvature, respectively. Switching ferroelastic order flips the direction of nonlinear SC and CC photocurrent by ±90°, while switching ferroelectric order flips both nonlinear photocurrents by 180°. In addition, changing left and right circular polarizations of light will induce 180° flip in CC. The microscopic understanding of nonlinear photocurrent switching from first-principles theory, together with very recent discoveries of 2D ferroics and multiferroics and ferroelectric inorganic perovskites and hybrid organic-inorganic perovskites, will open a variety of new avenues for tunable and configurable nonlinear optoelectronics, bulk photovoltaics, and nonlinear multiferroics, etc.

RESULTS

Theory of SC and CC

Ferroicity-driven nonlinear photocurrent switching originates from the second-order photo-induced DC density $\langle \boldsymbol{J}_{\mathrm{DC}} \rangle^{(2)}$. Unlike linear photocurrent, the direction of $\langle \boldsymbol{J}_{\mathrm{DC}} \rangle^{(2)}$ depends on intrinsic ferroic orders, which is the key to ferroicity-driven nonlinear photocurrent switching. $\langle \boldsymbol{J}_{\mathrm{DC}} \rangle^{(2)}$ consists of two types of nonlinear photocurrents, SC and CC, which reflect the polarization change upon photoexcitation per unit volume

$$\langle \boldsymbol{J}_{\mathrm{DC}} \rangle^{(2)} = \langle \boldsymbol{J}_{\mathrm{SC}} \rangle^{(2)} + \langle \boldsymbol{J}_{\mathrm{CC}} \rangle^{(2)} \tag{1}$$

where

$$\langle J^a_{\mathrm{SC}} \rangle^{(2)} = 2\sigma_2^{abc}(0;\omega,-\omega)E^b(\omega)E^c(-\omega) \tag{2}$$

$$\frac{d\langle J^a_{\mathrm{CC}} \rangle^{(2)}}{dt} = -2\mathrm{Im}\,\eta_2^{abc}(0;\omega,-\omega)\,|E^b(\omega)|\,|E^c(-\omega)|\sin(\varphi^b-\varphi^c) \tag{3}$$

Here, a, b, and c are Cartesian indices. The electric field can be described using phasors $\boldsymbol{E}(t) = \boldsymbol{E}(\omega)\exp(-i\omega t) + c.c.$ For the linearly polarized light, $\boldsymbol{E}(\omega)$ is real, while for left and right circularly polarized light, $\boldsymbol{E}(\omega)$ is complex, $E^b(\omega) = |E^b(\omega)|e^{i\varphi^b}$, with $\varphi^b - \varphi^c = \pm\frac{\pi}{2}$. We denote CC by $J^{a,\circlearrowleft}_{\mathrm{CC}}$ and $J^{a,\circlearrowright}_{\mathrm{CC}}$ for left and right circularly polarized light, respectively, and SC by $J^{a,\leftrightarrow}_{\mathrm{SC}}$ and $J^{a,\updownarrow}_{\mathrm{SC}}$ for linearly x- and y-polarized light, respectively.

The SC susceptibility tensor σ_2^{abc} can be derived from perturbation theory (*25*) as

$$\sigma_2^{abc}(0;\omega,-\omega) = \frac{i\pi e^3}{2\hbar^2}\int[d\boldsymbol{k}]\sum_{nm\sigma} f_{nm}\left(r^b_{mn}(r^c_{nm})_{;k^a} + r^c_{mn}(r^b_{nm})_{;k^a}\right)\delta(\omega_{mn}-\omega) \tag{4}$$

where $(r^b_{nm})_{;k^a} = \frac{\partial r^b_{nm}}{\partial k^a} - ir^b_{nm}(\mathcal{A}^a_n - \mathcal{A}^a_m)$ is the gauge covariant derivative. $\boldsymbol{r}_{nm} = i\langle n \mid \partial_{\boldsymbol{k}} \mid m\rangle$ and $\mathcal{A}_n = i\langle n \mid \partial_{\boldsymbol{k}} \mid n\rangle$ are interband and intraband Berry connections, respectively. f is the Fermi-Dirac distribution with $f_{nm} \equiv f_n - f_m$, and $\hbar\Delta^a_{mn} \equiv v^a_{mm} - v^a_{nn}$ is the group velocity difference of bands m and n. $[d\boldsymbol{k}] \equiv \frac{d\boldsymbol{k}}{(2\pi)^d}$ for d dimension. The SC susceptibility tensor under the linearly polarized light can be rewritten in a more elegant expression

$$\sigma_2^{abb}(0;\omega,-\omega) = -\frac{\pi e^3}{2\hbar^2}\int[d\boldsymbol{k}]\sum_{nm\sigma} f_{nm}R^{a,b}_{nm}(\boldsymbol{k})r^b_{nm}r^b_{mn}\delta(\omega_{mn}-\omega) \tag{5}$$

where $R^{a,b}_{nm}(\boldsymbol{k}) = -\frac{\partial\phi^b_{nm}(\mathbf{k})}{\partial k^a} + \mathcal{A}^a_n(\boldsymbol{k}) - \mathcal{A}^a_m(\boldsymbol{k})$ is the shift vector and $\phi_{nm}(\boldsymbol{k})$ is the phase factor of the Berry connection $r^b_{nm}(\boldsymbol{k}) = |r^b_{nm}(\boldsymbol{k})|e^{i\phi^b_{nm}(\boldsymbol{k})}$. $r^b_{nm}r^b_{mn}$ is the optical absorption strength. Hence, SC is determined by the product of linear photoabsorption and shift vector integrated over the Brillouin zone.

The CC susceptibility tensor η_2^{abc} (*25*) is given by

$$\eta_2^{abc}(0;\omega,-\omega) = -\frac{\pi e^3}{2\hbar^2}\int[d\boldsymbol{k}]\sum_{nm\sigma}\Delta^a_{nm}f_{nm}[r^b_{mn},r^c_{nm}]\delta(\omega_{mn}-\omega) \tag{6}$$

where $[r^b_{mn},r^c_{nm}] \equiv r^b_{mn}r^c_{nm} - r^c_{mn}r^b_{nm}$, indicating that CC vanishes under the linearly polarized light. It can be rewritten in a general form, assuming that light propagates along z

$$\eta_2^{a,z}(0;\omega,-\omega) = \frac{i\pi e^3}{2\hbar^2}\int[d\boldsymbol{k}]\sum_{nm\sigma}f_{nm}\Delta^a_{nm}\Omega^z_{mn}(\boldsymbol{k})\delta(\omega_{mn}-\omega) \tag{7}$$

where $\Omega^z_{mn}(\boldsymbol{k}) \equiv i[r^x_{mn},r^y_{nm}] = -i[r^y_{mn},r^x_{nm}]$ is the local Berry curvature between bands m and n. The global one reads $\Omega^z_m = \Sigma_{n\neq m}\Omega^z_{mn}$. It is clear to see that $\eta_2^{abc} = -\eta_2^{acb}$. The original "$bc$" indices in the CC susceptibility tensor are now absorbed in the index "z".

SC and CC involve distinct physical processes. Figure 1 shows the corresponding microscopic picture using a two-band model. SC arises from the displacement of wave packet upon photoabsorption, while CC stems from the asymmetric transport of electrons and holes and the self-rotation of the wave packet. The latter induces orbital magnetic momentum coupled with the circularly polarized light. The intrinsic permutation symmetry of the electric field leads to $\chi_2^{abc}(-\omega_m-\omega_n;\omega_m,\omega_n) = \chi_2^{acb}(-\omega_m-\omega_n;\omega_n,\omega_m)$, where χ_2^{abc} is a general second-order suseptibility. If time-reversal symmetry is also present, then

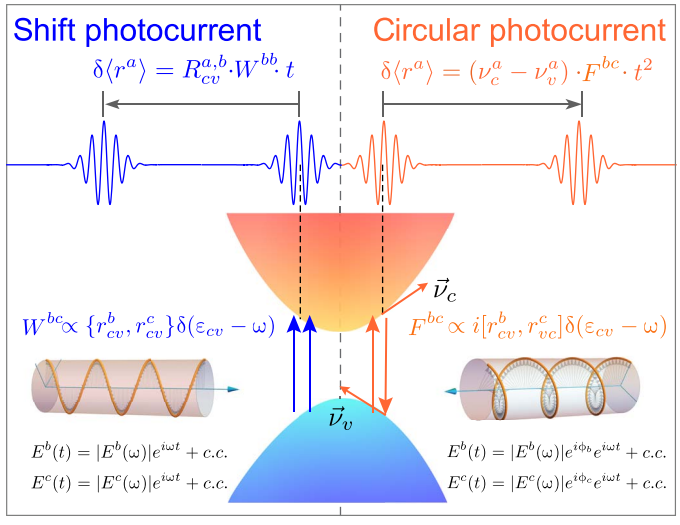

Fig. 1. Microscopic interpretation of SC and CC using a two-band model. $\delta\langle r^a\rangle$ is the variation of the mean value of position operator indicating the shift of electron wave packet in real space. Photoexcitation induces the shift of the electron wave packet in real space. SC comes from the displacement of wave packet upon photoabsorption, while CC stems from the asymmetric motion of electrons and holes and the self-rotation of the wave packet. The latter induces itinerant orbital magnetic momentum coupled with the circularly polarized light. Transition rate W of SC is proportional to the linear optical absorption strength under the linearly polarized light at frequency ω, while transition rate F of CC is proportional to the local Berry curvature under the circularly polarized light at frequency ω.

Downloaded from http://advances.sciencemag.org/ on January 17, 2021

$r^b_{nm}(-\boldsymbol{k}) = r^b_{mn}(\boldsymbol{k})$, $R^{a,b}_{nm}(-\boldsymbol{k}) = -R^{a,b}_{mn}(\boldsymbol{k}) = R^{a,b}_{nm}(\boldsymbol{k})$, and $\boldsymbol{\Omega}^z_{mn}(\boldsymbol{k}) = -\boldsymbol{\Omega}^z_{mn}(-\boldsymbol{k})$. As a result of the causality and permutation symmetry, $\eta_2^{abc}(0;\omega,-\omega) = \eta_2^{acb}(0;-\omega,\omega) = -\eta_2^{abc}(0;-\omega,\omega) = [\eta_2^{abc}(0;-\omega,\omega)]^*$, ensuring that η_2^{abc} is purely imaginary. In contrast, $\sigma_2^{abc}(0;\omega,-\omega) = \sigma_2^{acb}(0;-\omega,\omega) = \sigma_2^{abc}(0;-\omega,\omega) = [\sigma_2^{abc}(0;\omega,-\omega)]^*$, suggesting that σ_2^{abc} is purely real.

Relation between SC and CC

Although SC and CC have different physical meaning, they are closely related. The derivative of CC susceptibility tensor $\eta_2^{a,z}$ in Eq. 7 can be written as the following

$$\partial_\omega \eta_2^{a,z}(0;\omega,-\omega) = \frac{i\pi e^3}{2\hbar^2}\int [d\boldsymbol{k}] \sum_{nm\boldsymbol{\sigma}} f_{nm}(\partial_{k^a}\Omega^z_{mn})\delta(\omega_{mn}-\omega) \quad (8)$$

where the integration by parts is applied. Here, $\partial_{k^a}\Omega^z_{mn}$ is the Berry curvature dipole. Furthermore,

$$\nabla_{\boldsymbol{k}} \times \boldsymbol{R}_{mn}\cdot\hat{\boldsymbol{z}} = \frac{\partial R^{y,a}_{mn}(\boldsymbol{k})}{\partial k^x} - \frac{\partial R^{x,a}_{mn}(\boldsymbol{k})}{\partial k^y} = \Omega^z_m - \Omega^z_n \quad (9)$$

It shows that the two topological quantities, shift vector and Berry curvature, are closely connected. For a two-band model, $\Omega^z_m - \Omega^z_n = 2\Omega^z_{mn}$, thus

$$\partial_\omega \eta_2^{a,z}(0;\omega,-\omega) = \frac{-i\pi e^3}{4\hbar^2}\int [d\boldsymbol{k}] \sum_{\boldsymbol{\sigma}} \nabla_{k^a}(\nabla_{\boldsymbol{k}} \times \boldsymbol{R}_{vc}\cdot\hat{\boldsymbol{z}})\delta(\omega_{cv}-\omega) \quad (10)$$

Therefore, both SC and the derivative of CC with respect to frequency are related to the shift vector and hence the Berry curvature. The derivative of susceptibility $\partial_\omega \eta_2^{a,z}$ will contribute to the temporal response of rectification current rate when a short laser pulse is applied (*30*).

First-principles calculation and group theoretical analysis of SC in 2D multiferroic MX

The symmetry property of linear susceptibility and nonlinear SC and CC susceptibility is governed by point group and permutation symmetry, which correspond to direct product $\Gamma_{\boldsymbol{P}} \otimes \Gamma_{\boldsymbol{E}}$, $\Gamma_{J_{SC}} \otimes \Gamma_{\boldsymbol{EE}}$, and $\Gamma_{J_{CC}} \otimes \Gamma_{\boldsymbol{E}\times\boldsymbol{E}^*}$, respectively. Here, we take monolayer group IV monochalcogenides [MX, with M = (Ge, Sn) and X = (Se, S)] as an example, which is a ferroelectric-ferroelastic multiferroics (*29*). In 2D MX with C_{2v} point group (see Fig. 2, A and B, for crystal and electronic structure, respectively) and its character table (table S1), we have $\Gamma_{\boldsymbol{P}} \otimes \Gamma_{\boldsymbol{E}} = 3A_1 + 2A_2 + 2B_1 + 2B_2$. Notice that the coordinate system here is different from the conventional one in table S1. Hence, there are three independent nonzero components in linear susceptibilities. The permutation symmetry further separates them into symmetric and asymmetric representations (*31*), $\Gamma_{\boldsymbol{P}} \otimes \Gamma_{\boldsymbol{E}} = \Gamma^s + \Gamma^a$, where $\Gamma^s = 3A_1 + A_2 + B_1 + B_2$ and $\Gamma^a = A_2 + B_1 + B_2$. Moreover, because polarization $\boldsymbol{P}$, current $\boldsymbol{J}$, and electric field $\boldsymbol{E}$ are all polar vectors, they share the same representation; thus, $\Gamma_{J_{SC}} \otimes \Gamma_{\boldsymbol{EE}} = 7A_1 + 6A_2 + 7B_1 + 7B_2$ and $\Gamma_{J_{SC}} \otimes \Gamma^s_{EE} = 5A_1 + 3A_2 + 5B_1 + 5B_2$. As a result, there are five independent nonzero components in the SC susceptibility tensor. Figure 2 (C and D) shows two of the five nontrivial frequency-dependent SC susceptibilities $\sigma_2^{yxx}(0;\omega,-\omega)$ and $\sigma_2^{yyy}(0;\omega,-\omega)$ in 2D MX, where linearly *x*- and *y*-polarized light are considered. The corresponding SC along *y* direction reads $J^{y,\leftrightarrow}_{SC} = 2\,\sigma_2^{yxx}E^xE^x$ and $J^{y,\updownarrow}_{SC} = 2\,\sigma_2^{yyy}E^yE^y$, respectively. The SC for monolayer GeS agrees well with the results in (*21*, *32*). Furthermore, as shown in Fig. 2 (C and D), spin-orbit coupling (SOC) only slightly affects the SC in the case of GeS because of the weak spin-orbit interaction strength of Ge and S atoms. σ_2^{yyy} has two peaks below a frequency of 3 eV. The first peak at 2 eV (denoted by red circle in Fig. 2C) is contributed from the *k* points around the Brillouin zone center (Γ point). The second peak at 2.8 eV denoted by green circle is apparently very strong. It comes from the transition at the *k* points around the Brillouin zone boundary (*X* point) in a butterfly shape as shown in Fig. 2C. However, SOC can have notable impact in other cases such as well-known 1*H*-$MoSe_2$ and WSe_2, and the results for all MX and MX_2 without and with SOC are shown in figs. S1 and S2, respectively.

The reciprocal vector-dependent contributions to SC are shown in Fig. 2 (E and F) for photon energy of 2.0 and 2.8 eV, respectively. They are determined by the product of SC susceptibility density, $\mathrm{Im}[r^b_{vc}r^b_{cv;k^a}]$ (Fig. 2, G and J, for 2.0 and 2.8 eV, respectively), and the energy conservation law is carried by $\delta(\omega_{cv}-\omega)$. The distribution of SC susceptibility density can be further understood by focusing on the frequency-independent terms determined by the product of dipole transition strength, $r^b_{vc}r^b_{cv}$ (i.e., optical absorption), and shift vector $R^{a,b}_{nm}(\boldsymbol{k})$, as shown in Fig. 2 (H and I and K and L) for 2.0 and 2.8 eV, respectively. Im $r^x_{vc}r^x_{cv}$ vanishes at the *k* points around the band gap, while Im $r^y_{vc}r^y_{cv}$ remains finite because of the optical selection rule. $R^{a,b}_{nm}(\boldsymbol{k})$ is a gauge invariant topological quantity, which is well defined away from optical zero points, i.e., $r^b_{nm}(\boldsymbol{k})\neq 0$. Because the optical zero points have no contribution to SC, we compute the shift vector by

$$R^{a,b}_{nm}(\boldsymbol{k}) = \frac{1}{|r^b_{nm}|^2}\mathrm{Im}[r^b_{mn}r^b_{nm;k^a}] \quad (11)$$

The quantitative relationship between shift vector and polarization difference was recently reported (*33*). In the presence of time-reversal symmetry, $r^b_{nm}(-\boldsymbol{k}) = r^b_{mn}(\boldsymbol{k})$, $(r^b_{nm}(-\boldsymbol{k}))_{;k^a} = -(r^b_{mn}(\boldsymbol{k}))_{;k^a}$, which leads to $R^{a,b}_{nm}(-\boldsymbol{k}) = -R^{a,b}_{mn}(\boldsymbol{k}) = R^{a,b}_{nm}(\boldsymbol{k})$. This is confirmed in Fig. 2 (I and L). The shift vector can reach as high as ~15 Å, much larger than its lattice constant. This is very different from electric polarization vector, which is smaller than the lattice vector. Figures S3 and S4 show the distribution of the SC susceptibility tensor elements for monolayer $MoSe_2$ in the first Brillouin zone, demonstrating that its shift vector defined in Eq. 11 can go beyond its lattice parameter.

First-principles calculation and group theoretical analysis of CC in 2D multiferroic MX

For the circularly polarized light along *z*, $(\boldsymbol{E}\times\boldsymbol{E}^*)_z$ and axial axis R_z share the B_2 representation. Therefore, $\Gamma_{\boldsymbol{j}^*} \otimes \Gamma_{R_z} = B_2 \otimes B_2 = A_1$, indicating that there is a nonzero CC response along *x* direction $\eta_2^{x,z}(0;\omega,-\omega)$ when the applied circularly polarized light is along the *z* direction, i.e., perpendicular to 2D plane. Figure 3 (A and B) shows two antisymmetric CC susceptibility tensor elements, Im η_2^{xxy} and Im η_2^{xyx}, respectively. Unlike SC, the main response of CC spread into two peaks from 2 to 6 eV. The peak values of Im η_2^{abc} in the four MX materials are about 100 to 300 × 10^8 nm $AV^{-2}s^{-1}$, which allows us to estimate the generated nonlinear CC under continuous wave limit as follows. At room temperature, a typical relaxation time of the electrons in MX

Downloaded from http://advances.sciencemag.org/ on January 17, 2021

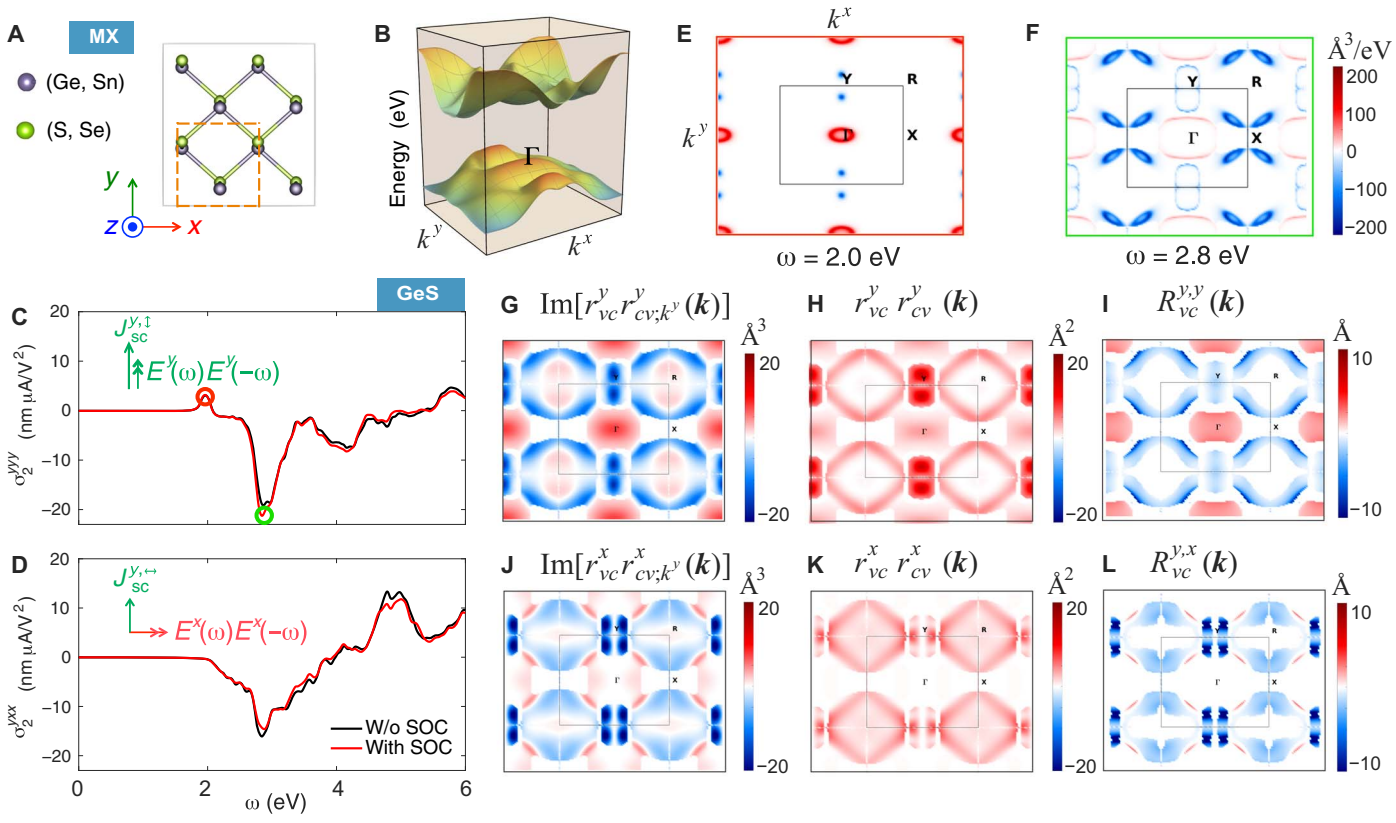

Fig. 2. SC and its microscopic origin in 2D ferroelastic-ferroelectric monolayer group IV monochalcogenide GeS. (**A**) Crystal structure of monolayer group IV monochalcogenides MX, where M = (Ge, Sn) and X = (S, Se). (**B**) 2D electronic band structure near the Fermi level. (**C** and **D**) Frequency-dependent nonlinear SC response to incoming linearly *x*- and *y*-polarized light, respectively. (**E** and **F**) Reciprocal vector ***k***-resolved SC susceptibility under linearly *y*-polarized light at the first two peaks (2.0 and 2.8 eV). (**G** to **L**) ***k***-resolved SC strength (G and J), ***k***-resolved dipole transition strength (H and K), and ***k***-resolved topological shift vector of 2D GeS in 2D Brillouin zone under linearly *x*- and *y*-polarized light, respectively (I and L).

materials is around $\tau = \mu_e/\left(\frac{e}{m^*}\right) \sim 10^{-14}$s (*34*). μ_e is the mobility, and m^* is the effective mass of electrons. Considering a regular laser pointer with an intensity of 1 mW/cm^2 and a 2D MX with an effective thickness of 1 nm, the induced CC J_{CC} can reach up to 10 to 30 μA/cm^2, indicating that the current can even be observed using low-power continuous wave source (sheet photocurrent of 10 to 30 nm $\frac{\mu A}{cm^2}$, i.e., 100 to 300 pA/m) (*35*). SC and CC are generated simultaneously under the circularly polarized light. It is possible to compare their peak amplitudes if we assume the same incident light intensity and a relaxation time of 10^{-14}s for GeS. CC is larger than SC, $J_{CC}/J_{SC} \sim 5$. The second-order nonlinear photocurrent response for different incident polarized light is summarized in table S2. Note that there is another nonzero element $\eta_2^{z,x}(0;\omega,-\omega)$ in the CC susceptibility tensor because $\Gamma_{j^z} \otimes \Gamma_{R_x} = B_1 \otimes B_1 = A_1$, suggesting that there exists a CC response along the *z* direction when the incoming circularly polarized light is along the *x* direction.

Figure 3 (C and D) shows the ***k***-resolved CC susceptibility in monolayer GeS under the circularly polarized light at two different frequencies (2.3 and 2.8 eV), demonstrating that the main response of the CC is localized around *Y* point. Note that, for the same frequency of 2.8 eV, the SC (Fig. 2F) and CC (Fig. 3D) are very different from each other, as the SC is localized around the *Y* point. The CC susceptibility is determined by the product of group velocity difference and Berry curvature $\boldsymbol{\Omega}^z_{cv}(\boldsymbol{k})$. The susceptibility tensor relates the component of the polar vector ***J*** and the axial vector $\mathbf{e} \times \mathbf{e}^*$. Hence, it is nonzero for the point groups that allow optical activity or gyrotropy. Here, **e** is the unit vector of light polarization. Figure 3E shows the group velocity difference between the highest valence band and the lowest conduction band, which confirms the time-reversal symmetry $\boldsymbol{\Delta}(\boldsymbol{k}) = -\boldsymbol{\Delta}(-\boldsymbol{k})$ (see figs. S5 and S6 for the energy-dependent group velocity distribution). The Berry curvature $\boldsymbol{\Omega}^z_{cv}(\boldsymbol{k})$ of GeS is shown in Fig. 3F, which confirms that $\boldsymbol{\Omega}^z_{cv}(\boldsymbol{k}) = -\boldsymbol{\Omega}^z_{cv}(-\boldsymbol{k})$ under time-reversal symmetry and that the mirror plane (*yz* plane) leads to opposite Berry curvature at $(\pm k^x, k^y)$. The product of these two odd functions, $\boldsymbol{\Delta}(\boldsymbol{k})$ and $\boldsymbol{\Omega}^z_{cv}(\boldsymbol{k})$, results in nonvanishing CC in 2D MX with C_{2v} point group. This is in direct contrast to 1*H*-$MoSe_2$, whose CC response vanishes because of its D_{3h} point group (see character table in table S1), as evident in its Berry curvature shown in fig. S7.

Ferroicity-driven nonlinear photocurrent switching

The above group theoretical analyses and first-principles calculations illustrate the underlying selection rule and microscopic mechanism governing nonlinear SC and CC photocurrents. Because they are intimately related to the symmetry and topology, nonlinear SC and CC photocurrents are inherently coupled with the intrinsic ferroic orders in 2D multiferroics MX, giving rise to ferroicity-driven nonlinear photocurrent switching, which we will discuss below. Let us first inspect the coupling between ferroelectric order (P_y) and nonlinear SC and CC responses. Because both CC and SC are polar vectors, the sign of SC will flip upon ferroelectric polarization switch ($P_y \rightarrow -P_y$). Consequently, the

Downloaded from http://advances.sciencemag.org/ on January 17, 2021

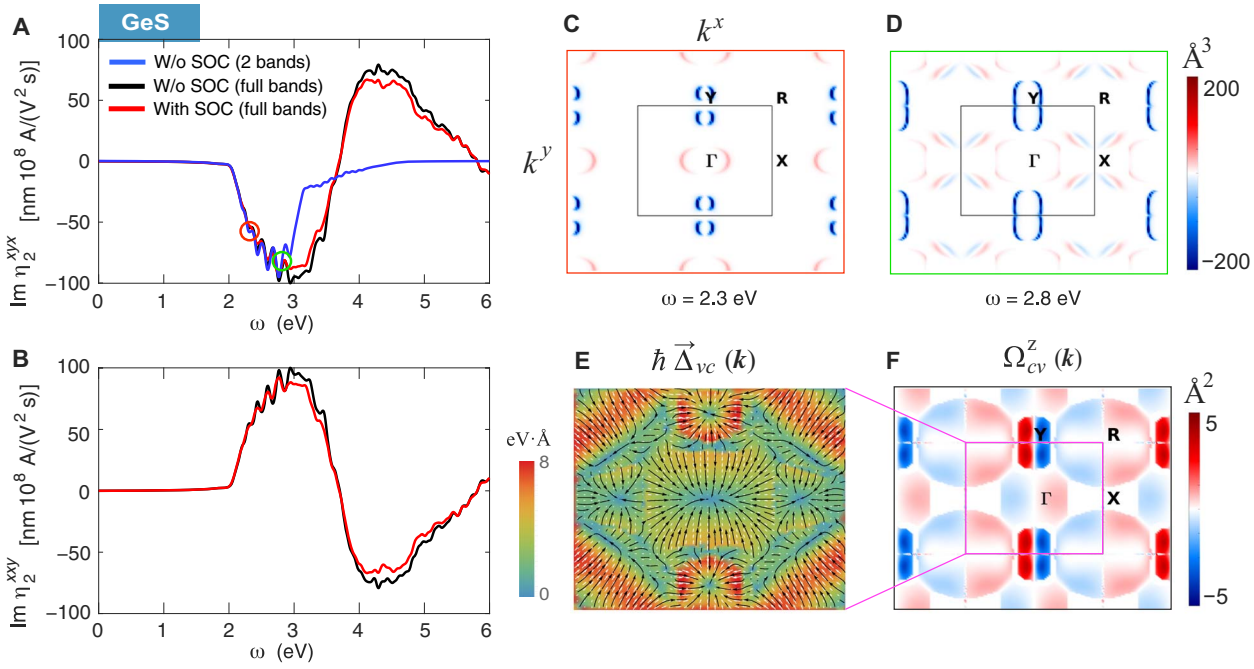

Fig. 3. CC and its microscopic origin in 2D ferroelastic-ferroelectric monolayer group IV monochalcogenide GeS. (**A** and **B**) Two opposite CC susceptibility tensor elements induced by the circularly polarized light. (**C** and **D**) Evolution of reciprocal vector ***k***-resolved CC susceptibility under the circularly polarized light at two different frequencies (2.3 and 2.8 eV). (**E** and **F**) Group velocity difference and Berry curvature between the highest valence band and the lowest conduction band. The white arrows in (E) denote the calculated group velocity difference at specific ***k*** point, and the black curves indicate the associated stream lines.

sign of SC susceptibility tensor $\sigma_2^{ybb}(0;\omega,-\omega)$ and CC susceptibility tensor $\eta_2^{x,z}(0;\omega,-\omega)$ will also flip. Thus, under the same linearly and circularly polarized light, SC and CC will change the direction by 180° upon ferroelectric polarization switch, i.e., $J_{\mathrm{SC}}^{y,\leftrightarrow}(P_y)=-J_{\mathrm{SC}}^{y,\leftrightarrow}(-P_y)$, $J_{\mathrm{SC}}^{y,\updownarrow}(P_y)=-J_{\mathrm{SC}}^{y,\updownarrow}(-P_y)$, $J_{\mathrm{CC}}^{x,\circlearrowleft}(P_y)=-J_{\mathrm{CC}}^{x,\circlearrowleft}(-P_y)$, and $J_{\mathrm{CC}}^{x,\circlearrowleft}(P_y)=-J_{\mathrm{CC}}^{x,\circlearrowleft}(-P_y)$. This property can be obtained from microscopic theory by considering the transformation rules of different matrix elements under space inversion and time-reversal operation, including interband Berry connections $\boldsymbol{r}_{mn}(\boldsymbol{k})$, shift vector $\boldsymbol{R}_{mn}(\boldsymbol{k})$, group velocity difference $\boldsymbol{\Delta}_{mn}(\boldsymbol{k})$, and Berry curvature $\boldsymbol{\Omega}_{mn}(\boldsymbol{k})$ as listed in Table 1.

Next, we examine the coupling between ferroelastic order (e.g., spontaneous strain $\epsilon_{yy}>0$ and $\epsilon_{xx}<0$) and nonlinear photocurrent responses. Upon ferroelastic transition ($\epsilon_{yy}\rightarrow\epsilon_{xx}$ and $\epsilon_{xx}\rightarrow\epsilon_{yy}$), shift vector $R_{nm}^{y,b}(\boldsymbol{k})$, Berry curvature $\Omega_{mn}^{z}(\boldsymbol{k})$, $r_{nm}^{b}r_{mn}^{b}$, and Δ_{nm}^{a} will all rotate by 90°, which effectively switches the *xy* index. As a result, under the same linearly and circularly polarized light, nonlinear SC and CC photocurrent will change their direction by 90° upon ferroelastic transition, i.e., $J_{\mathrm{SC}}^{y,\leftrightarrow}(\epsilon_{yy})=J_{\mathrm{SC}}^{x,\updownarrow}(\epsilon_{xx})$, $J_{\mathrm{SC}}^{y,\updownarrow}(\epsilon_{yy})=J_{\mathrm{SC}}^{x,\leftrightarrow}(\epsilon_{xx})$, $J_{\mathrm{CC}}^{y,\circlearrowleft}(\epsilon_{yy})=J_{\mathrm{CC}}^{x,\circlearrowleft}(\epsilon_{xx})$, and $J_{\mathrm{CC}}^{x,\circlearrowleft}(\epsilon_{yy})=J_{\mathrm{CC}}^{x,\circlearrowleft}(\epsilon_{xx})$. Note that, in general, $J_{\mathrm{CC}}^{\circlearrowleft}=-J_{\mathrm{CC}}^{\circlearrowleft}$, $J_{\mathrm{SC}}^{y,\leftrightarrow}$, and $J_{\mathrm{SC}}^{y,\updownarrow}$ are independent. However, $J_{\mathrm{SC}}^{y,\leftrightarrow}=-J_{\mathrm{SC}}^{y,\updownarrow}$ holds in group D_{3h}, with a mirror plane perpendicular to *x* axis, e.g., 1*H*-$MoSe_2$.

Because 2D MX has both ferroelectric and ferroelastic orders, it has four multiferroic ($\pm P$, $\pm\epsilon$) states, whose nonlinear photocurrent SC and CC are directly correlated as listed in Table 2. Here, we define ferroelastic strain $+\epsilon$ for $\epsilon_{xx}<0$ and $\epsilon_{yy}>0$ and $-\epsilon$ for $\epsilon_{xx}>0$ and $\epsilon_{yy}<0$. Ferroelectric polarization *P* could be $\pm P_x$ if $\epsilon_{xx}>0$ or $\pm P_y$ if $\epsilon_{yy}>0$. In contrast, linear optical susceptibility will not change with ferroelectric polarization switching because its matrix element $r_{nm}^{b}r_{mn}^{b}$ is always positive. Moreover, for a given multiferroic state (P, ϵ), nonlinear SC and CC current responses in 2D MX are bulk photocurrent response along different directions; thus, SC and CC can serve as a fundamental principle for real-space mapping of ferroelectric and ferroelastic orders.

DISCUSSION

The above group theoretical analysis and first-principles calculations can be generally applied to other ferroic materials that can host ferroicity-driven nonlinear photocurrent switching. We can extend the above analysis to all 32 crystallographic point groups. There are 21 noncentrosymmetric point groups, 10 of which (C_1, C_s, C_n, C_{nv}, $n=2,3,4,6$) have polar axis, a necessary but insufficient condition for ferroelectric materials. Assuming *z* to be the polar axis, *z* will transform as the total symmetric representation; therefore, $\Gamma_{j^z}\otimes\Gamma_{E^x}\otimes\Gamma_{E^x}$ and $\Gamma_{j^z}\otimes\Gamma_{E^y}\otimes\Gamma_{E^y}$ always contain the total symmetric representation, indicating that nonvanishing SC is perpendicular to electric field and thus leads to a nonlinear transverse photocurrent. This transverse current cannot be observed from conventional linear Hall effect in time-reversal invariant materials. Furthermore, 18 of 21 noncentrosymmetric point groups including all the 10 polar classes are gyrotropic; hence, they all have nonvanishing CC.

Although our focus here is on the ferroicity-driven nonlinear photocurrent switching based on interband process–induced second-order photocurrent, the similar effect can be also found in ferroelectric semimetals where static and low-frequency electric field–induced nonlinear Hall current can be switched upon ferroelectric switching. However, it should be emphasized that not all ferroic materials exhibit nonlinear photocurrent switching upon ferroic transition. Similar to the present case, it depends on the underlying symmetry transformation of ferroelectric transition. More excitingly, it can be readily extended to higher-order or other types of nonlinear effects, e.g., optically induced

Downloaded from http://advances.sciencemag.org/ on January 17, 2021

Table 1. Transformation of interband Berry connection $\mathbf{r}_{mn}$, shift vector $\mathbf{R}_{mn}$, group velocity difference Δ_{mn}, and Berry curvature Ω_{mn} under space inversion $\mathcal{I}$ and time reversal $\mathcal{T}$ symmetry operation. $R_{mn}(\boldsymbol{k})$ is odd under $\mathcal{I}$ and even under $\mathcal{T}$ in moment space. $\Omega_{mn}(\boldsymbol{k})$ is even under $\mathcal{I}$ and odd under $\mathcal{T}$ in moment space. These transformation rules govern the coupling between ferroelectric polarization and nonlinear SC and CC photocurrent: $J^{y,\leftrightarrow}_{SC}(P_y) = -J^{y,\leftrightarrow}_{SC}(-P_y)$, $J^{y,\updownarrow}_{SC}(P_y) = -J^{y,\updownarrow}_{SC}(-P_y)$, $J^{x,\circlearrowleft}_{CC}(P_y) = -J^{x,\circlearrowleft}_{CC}(-P_y)$, and $J^{x,\circlearrowleft}_{CC}(P_y) = -J^{x,\circlearrowleft}_{CC}(-P_y)$.

Quantity	Symmetry operation		Gauge dependency
	Space inversion ($\mathcal{I}$)	Time reversal ($\mathcal{T}$)	
$\boldsymbol{r}_{mn}(\boldsymbol{k})$	$-\boldsymbol{r}_{mn}(-\boldsymbol{k})$	$\boldsymbol{r}^{*}_{mn}(-\boldsymbol{k})$	Yes
$\boldsymbol{R}_{mn}(\boldsymbol{k})$	$-\boldsymbol{R}_{mn}(-\boldsymbol{k})$	$\boldsymbol{R}_{mn}(-\boldsymbol{k})$	No
$\Delta_{mn}(\boldsymbol{k})$	$-\Delta_{mn}(-\boldsymbol{k})$	$-\Delta_{mn}(-\boldsymbol{k})$	No
$\Omega_{mn}(\boldsymbol{k})$	$\Omega_{mn}(-\boldsymbol{k})$	$-\Omega_{mn}(-\boldsymbol{k})$	No

Table 2. Ferroicity-driven nonlinear photocurrent switching. Second-order nonlinear photocurrent SC and CC responses are directly correlated with the intrinsic ferroic orders ($\pm P$, $\pm\epsilon$) of 2D MX materials and external linear ($\leftrightarrow$, $\updownarrow$) and circular ($\circlearrowleft$, $\circlearrowright$) polarization of incoming light. A total of 16 types of in-plane nonlinear photocurrents can be generated by controlling four ferroic states and four types of light polarizations.

Nonlinear photocurrent (J^{x}, J^{y})			Ferroelectric order			
			$+P$		$-P$	
			$+P_x$ if $\epsilon_{xx} > 0$	$+P_y$ if $\epsilon_{yy} > 0$	$-P_x$ if $\epsilon_{xx} > 0$	$-P_y$ if $\epsilon_{yy} > 0$
Ferroelastic order	$+\epsilon$	$\epsilon_{xx} < 0$ and $\epsilon_{yy} > 0$	$(J^{\circlearrowleft,\circlearrowleft}_{CC}, J^{\leftrightarrow,\updownarrow}_{SC})$		$(-J^{\circlearrowleft,\circlearrowleft}_{CC}, -J^{\leftrightarrow,\updownarrow}_{SC})$	
	$-\epsilon$	$\epsilon_{xx} > 0$ and $\epsilon_{yy} < 0$	$(J^{\updownarrow,\leftrightarrow}_{SC}, J^{\circlearrowleft,\circlearrowleft}_{CC})$		$(-J^{\updownarrow,\leftrightarrow}_{SC}, -J^{\circlearrowleft,\circlearrowleft}_{CC})$	

nonlinear magnetization switching and ferroicity-driven third-order nonlinear photocurrent switching. It will offer unprecedented opportunities for nonlinear optoelectronics, nonlinear optomagnetics, and nonlinear optoelectromagnetics, namely, nonlinear multiferroics, as potential routes to control polarization, charge current, magnetization, and spin current in an ultrafast, noninvasive manner without the stringent requirement of strongly coupled lattice, polarization, and magnetization in conventional multiferroics.

In summary, using group theoretical analyses and first-principles calculations, we have studied the microscopic mechanism of nonlinear photocurrent switching in time-reversal invariant multiferroics. Our results show that nonlinear photocurrent is highly sensitive to the symmetry of materials, including point group symmetry and time-reversal symmetry. This leads to ferroicity-driven nonlinear photocurrent switching—unique to multiferroics where the direction of second-order photocurrent is strongly correlated with intrinsic ferroic orders and external light polarization. The concept of ferroicity-driven nonlinear photocurrent switching illustrated here is not limited to 2D multiferroics, rather it can be generally applicable to many ferroics (e.g., ferroelectric inorganic perovskites and hybrid organic-inorganic perovskites) and even ferroelectric metals. One can envisage to directly control nonlinear photocurrent by switching ferroelastic strain and/or ferroelectric polarization accompanied by instantaneous direction and/or sign switching of the photocurrent. Furthermore, one may conduct high-resolution characterization of ferroelastic and ferroelectric orders and domain evolution using ultrafast optical techniques based on ferroicity-dependent nonlinear photocurrent. The present findings thus will open up avenues for realizing configurable nonlinear optoelectronics, bulk photovoltaics, nonlinear multiferroics, etc., using their ferroic orders and various nonlinear responses under external field.

MATERIALS AND METHODS

First-principles atomistic and electronic structure calculations

Ground-state crystal structures of MX were calculated by first-principles density functional theory (DFT) (*36*, *37*) implemented in the Vienna Ab initio Simulation Package (VASP) (*38*, *39*) with the projector-augmented wave method (*40*) and a plane-wave basis with an energy cutoff of 400 eV. We used the generalized gradient approximation of exchange-correlation functional in the Perdew-Burke-Ernzerhof (*41*) form and a Monkhorst-Pack k-point sampling of $12 \times 12 \times 1$ for the Brillouin zone integration.

First-principles nonlinear SC and CC calculations

To evaluate the nonlinear photocurrent responses, we developed a nonlinear optical code interfaced with first-principles DFT packages (e.g., VASP and Quantum-ESPRESSO). Second-order nonlinear photocurrent responses such as SC and CC are different from linear optical absorption, as the numerical integration of generalized Berry connection has to be performed over the whole Brillouin zone and multiple band indices for 27 third-rank tensor elements at each frequency. We therefore parallelized and benchmarked the code with tensor symmetrization and SOC taken into account. For the present calculations, we found that a dense $72 \times 72 \times 1$ k-point sampling, 40 electronic bands

Downloaded from http://advances.sciencemag.org/ on January 17, 2021

without SOC (80 bands with SOC), and a total of 1000 frequency grids in an energy range of −6 to 6 eV are enough to achieve converged nonlinear photocurrent susceptibility tensors. The fundamental frequency ω in the denominator of susceptibility tensor carries a small imaginary smearing factor τ of 0.05 eV: $\omega \rightarrow \omega + i\tau$. We used the Sokhotski-Plemelj theorem to perform the integrals of Dirac delta function, which reads $\lim_{\tau\to 0} \frac{1}{\omega_{mn} \pm (\omega + i\tau)} = \mathcal{P} \frac{1}{\omega_{mn} \pm \omega} \mp i\pi\delta(\omega_{mn} \pm \omega)$. $\mathcal{P}$ is the Cauchy principal value. It should be emphasized that this formula is only meaningful when it is multiplied by a function and integrated over the first Brillouin zone and the real line including the point $\omega = \omega_{mn}$. This always holds true in our case. Last, the single-particle approximation often underestimates the bandgap, and two-body and higher-order interactions may also affect the results. To check the effect of the single-particle approximation, we applied a scissor operator to correct both bandgap and matrix elements by using the optical bandgap obtained from quasiparticle GW and Bethe-Salpeter equation calculations. This approach is a reasonable remedy as the GW and DFT band structures are similar for the MX materials. Figure S8 shows the nonlinear photocurrent calculated with and without the scissor operator, and the main effect is the relative shift of the peak positions with slightly reduced peak intensity. This is expected as it mostly affects the denominator and delta function in the equations for SC and CC. Two-body and higher-order excitations in principle can be taken into account by incorporating many-body wave functions (e.g., exciton wave functions as a linear combination of electron hole pair excitations) into the SC and CC tensors, which may change the SC and CC peak position and amplitude. Nonetheless, the main conclusions on the ferroicity-driven nonlinear photocurrent switching behavior from the symmetry analysis and first-principles calculations shall still hold, and future efforts shall be made to include the exciton and other high-order excitation effect.

SUPPLEMENTARY MATERIALS

Supplementary material for this article is available at http://advances.sciencemag.org/cgi/content/full/5/8/eaav9743/DC1

Table S1. Character table for C_{2v} and D_{3h}.

Table S2. Second-order nonlinear photocurrent responses under different polarized light.

Fig. S1. SC and CC in monolayer MX (C_{2v}) and 1*H*-MX_2 (D_{3h}) without SOC.

Fig. S2. SC and CC in monolayer MX (C_{2v}) and 1*H*-MX_2 (D_{3h}) with SOC.

Fig. S3. Microscopic distribution and frequency-dependent shift photocurrent susceptibility in monolayer 1*H*-$MoSe_2$ with D_{3h} point group.

Fig. S4. SC and its microscopic origin in monolayer 1*H*-$MoSe_2$.

Fig. S5. Group velocity v_x distribution in monolayer GeS.

Fig. S6. Group velocity v_y distribution in monolayer GeS.

Fig. S7. Berry curvature distribution in monolayer 1*H*-$MoSe_2$.

Fig. S8. SC susceptibility tensor elements ($\sigma^{(2)}_{yxx}$, $\sigma^{(2)}_{yyy}$) and CC susceptibility tensor elements ($\eta^{(2)}_{xyx}$, $\eta^{(2)}_{xxy}$) of monolayer GeS with and without the scissor operator.

REFERENCES AND NOTES

1. J. Weiner, F. Nunes, *Light-Matter Interaction: Physics and Engineering at the Nanoscale* (OUP, 2012).
2. C. Lienau, M. A. Noginov, M. Lončar, Light–matter interactions at the nanoscale. *J. Opt.* **16**, 110201 (2014).
3. J. Weiner, P.-T. Ho, *Light-Matter Interaction, Fundamentals and Applications* (John Wiley & Sons, 2008), vol. 1.
4. R. Thomson, C. Leburn, D. Reid, *Ultrafast Nonlinear Optics* (Springer, 2013).
5. C. L. Evans, X. S. Xie, Coherent anti-Stokes Raman scattering microscopy: Chemical imaging for biology and medicine. *Annu. Rev. Anal. Chem.* **1**, 883–909 (2008).
6. P. G. Kwiat, E. Waks, A. G. White, I. Appelbaum, P. H. Eberhard, Ultrabright source of polarization-entangled photons. *Phys. Rev. A* **60**, R773–R776 (1999).
7. N. Gisin, G. Ribordy, W. Tittel, H. Zbinden, Quantum cryptography. *Rev. Mod. Phys.* **74**, 145–195 (2002).
8. M. F. Yanik, S. Fan, M. Soljačić, J. D. Joannopoulos, All-optical transistor action with bistable switching in a photonic crystal cross-waveguide geometry. *Opt. Lett.* **28**, 2506–2508 (2003).
9. V. R. Almeida, C. A. Barrios, R. R. Panepucci, M. Lipson, All-optical control of light on a silicon chip. *Nature* **431**, 1081–1084 (2004).
10. C. Ríos, M. Stegmaier, P. Hosseini, D. Wang, T. Scherer, C. D. Wright, H. Bhaskaran, W. H. P. Pernice, Integrated all-photonic non-volatile multi-level memory. *Nat. Photonics* **9**, 725–732 (2015).
11. Y.-R. Shen, *The Principles of Nonlinear Optics* (Wiley-Interscience, 1984).
12. R. W. Boyd, *Nonlinear Optics* (Elsevier Inc., ed. 3, 2008).
13. T. Oka, H. Aoki, Photovoltaic Hall effect in graphene. *Phys. Rev. B* **79**, 081406 (2009).
14. L. Wu, S. Patankar, T. Morimoto, N. L. Nair, E. Thewalt, A. Little, J. G. Analytis, J. E. Moore, J. Orenstein, Giant anisotropic nonlinear optical response in transition metal monopnictide Weyl semimetals. *Nat. Phys.* **13**, 350–355 (2017).
15. T. Morimoto, N. Nagaosa, Topological nature of nonlinear optical effects in solids. *Sci. Adv.* **2**, e1501524 (2016).
16. G. B. Osterhoudt, L. K. Diebel, M. J. Gray, X. Yang, J. Stanco, X. Huang, B. Shen, N. Ni, P. J. W. Moll, Y. Ran, K. S. Burch, Colossal mid-infrared bulk photovoltaic effect in a type-I Weyl semimetal. *Nat. Mater.* **18**, 471–475 (2019).
17. F. de Juan, A. G. Grushin, T. Morimoto, J. E. Moore, Quantized circular photogalvanic effect in Weyl semimetals. *Nat. Commun.* **8**, 15995 (2017).
18. Q. Ma, S.-Y. Xu, C.-K. Chan, C.-L. Zhang, G. Chang, Y. Lin, W. Xie, T. Palacios, H. Lin, S. Jia, Direct optical detection of Weyl fermion chirality in a topological semimetal. *Nat. Phys.* **13**, 842–847 (2017).
19. M. Zhao, Z. Ye, R. Suzuki, Y. Ye, H. Zhu, J. Xiao, Y. Wang, Y. Iwasa, X. Zhang, Atomically phase-matched second-harmonic generation in a 2D crystal. *Light Sci. Appl.* **5**, e16131 (2016).
20. H. Wang, X. Qian, Giant optical second harmonic generation in two-dimensional multiferroics. *Nano Lett.* **17**, 5027–5034 (2017).
21. T. Rangel, B. M. Fregoso, B. S. Mendoza, T. Morimoto, J. E. Moore, J. B. Neaton, Large bulk photovoltaic effect and spontaneous polarization of single-layer monochalcogenides. *Phys. Rev. Lett.* **119**, 067402 (2017).
22. R. von Baltz, W. Kraut, Theory of the bulk photovoltaic effect in pure crystals. *Phys. Rev. B* **23**, 5590–5596 (1981).
23. S. M. Young, A. M. Rappe, First principles calculation of the shift current photovoltaic effect in ferroelectrics. *Phys. Rev. Lett.* **109**, 116601 (2012).
24. P. J. Sturman, V. M. Fridkin, *Photovoltaic and Photo-refractive Effects in Noncentrosymmetric Materials* (CRC Press, 1992), vol. 8.
25. J. E. Sipe, A. I. Shkrebtii, Second-order optical response in semiconductors. *Phys. Rev. B* **61**, 5337–5352 (2000).
26. J. E. Moore, J. Orenstein, Confinement-induced Berry phase and helicity-dependent photocurrents. *Phys. Rev. Lett.* **105**, 026805 (2010).
27. I. Sodemann, L. Fu, Quantum nonlinear Hall effect induced by Berry curvature dipole in time-reversal invariant materials. *Phys. Rev. Lett.* **115**, 216806 (2015).
28. K. Chang, J. Liu, H. Lin, N. Wang, K. Zhao, A. Zhang, F. Jin, Y. Zhong, X. Hu, W. Duan, Q. Zhang, L. Fu, Q.-K. Xue, X. Chen, S.-H. Ji, Discovery of robust in-plane ferroelectricity in atomic-thick SnTe. *Science* **353**, 274–278 (2016).
29. H. Wang, X. Qian, Two-dimensional multiferroics in monolayer group IV monochalcogenides. *2D Mater.* **4**, 015042 (2017).
30. F. Nastos, J. Sipe, Optical rectification and shift currents in GaAs and GaP response: Below and above the band gap. *Phys. Rev. B* **74**, 035201 (2006).
31. M. S. Dresselhaus, G. Dresselhaus, A. Jorio, *Group Theory: Application to the Physics of Condensed Matter* (Springer Science & Business Media, 2007).
32. C. Wang, X. Liu, L. Kang, B.-L. Gu, Y. Xu, W. Duan, First-principles calculation of nonlinear optical responses by Wannier interpolation. *Phys. Rev. B* **96**, 115147 (2017).
33. B. M. Fregoso, T. Morimoto, J. E. Moore, Quantitative relationship between polarization differences and the zone-averaged shift photocurrent. *Phys. Rev. B* **96**, 075421 (2017).
34. O. Madelung, *Semiconductors—Basic Data* (Springer Science & Business Media, 2012).
35. N. Laman, A. Shkrebtii, J. Sipe, H. Van Driel, Quantum interference control of currents in CdSe with a single optical beam. *Appl. Phys. Lett.* **75**, 2581–2583 (1999).
36. P. Hohenberg, W. Kohn, Inhomogeneous electron gas. *Phys. Rev. B* **136**, B864–B871 (1964).
37. W. Kohn, L. J. Sham, Self-consistent equations including exchange and correlation effects. *Phys. Rev.* **140**, A1133–A1138 (1965).
38. G. Kresse, J. Furthmüller, Efficient iterative schemes for ab initio total-energy calculations using a plane-wave basis set. *Phys. Rev. B* **54**, 11169–11186 (1996).

Downloaded from http://advances.sciencemag.org/ on January 17, 2021

39. G. Kresse, J. Furthmüller, Efficiency of ab-initio total energy calculations for metals and semiconductors using a plane-wave basis set. *Comput. Mater. Sci.* **6**, 15–50 (1996).
40. P. E. Blöchl, Projector augmented-wave method. *Phys. Rev. B* **50**, 17953–17979 (1994).
41. J. P. Perdew, K. Burke, M. Ernzerhof, Generalized gradient approximation made simple. *Phys. Rev. Lett.* **77**, 3865–3868 (1996).

Acknowledgments: Portions of this research were conducted with the advanced computing resources provided by Texas A&M High Performance Research Computing. **Funding:** This research was supported by the National Science Foundation (NSF) under award no. DMR-1753054. **Author contributions:** X.Q. conceived the project and supervised the research. H.W. performed the calculations. H.W. and X.Q. developed the first-principles codes for computing second-order nonlinear SC and CC, analyzed the results, and wrote the manuscript. **Competing interests:** The authors declare that they have no competing interests. **Data and materials availability:** All data needed to evaluate the conclusions in the paper are present in the paper and/or the Supplementary Materials. Additional data related to this paper may be requested from the corresponding author.

Submitted 6 November 2018
Accepted 10 July 2019
Published 16 August 2019
10.1126/sciadv.aav9743

Citation: H. Wang, X. Qian, Ferroicity-driven nonlinear photocurrent switching in time-reversal invariant ferroic materials. *Sci. Adv.* **5**, eaav9743 (2019).

Downloaded from http://advances.sciencemag.org/ on January 17, 2021

Science Advances

Ferroicity-driven nonlinear photocurrent switching in time-reversal invariant ferroic materials

Hua Wang and Xiaofeng Qian

Sci Adv **5** (8), eaav9743.
DOI: 10.1126/sciadv.aav9743

ARTICLE TOOLS http://advances.sciencemag.org/content/5/8/eaav9743

SUPPLEMENTARY MATERIALS http://advances.sciencemag.org/content/suppl/2019/08/12/5.8.eaav9743.DC1

REFERENCES This article cites 33 articles, 2 of which you can access for free
http://advances.sciencemag.org/content/5/8/eaav9743#BIBL

PERMISSIONS http://www.sciencemag.org/help/reprints-and-permissions

Use of this article is subject to the Terms of Service

Science Advances (ISSN 2375-2548) is published by the American Association for the Advancement of Science, 1200 New York Avenue NW, Washington, DC 20005. The title *Science Advances* is a registered trademark of AAAS.

Copyright © 2019 The Authors, some rights reserved; exclusive licensee American Association for the Advancement of Science. No claim to original U.S. Government Works. Distributed under a Creative Commons Attribution NonCommercial License 4.0 (CC BY-NC).

Downloaded from http://advances.sciencemag.org/ on January 17, 2021